Check for updates

CHEMISTRY
AN ASIAN JOURNAL

www.chemasianj.org

Accepted Article

Title: A Novel Solution-based Method for Synthesizing Pyrite-type Ferrous Metal Sulfide Microspheres with Efficient OER Activity

Authors: Wendi Xiang, Qianqiu Tian, Cheng Zhong, Yida Deng, Xiaopeng Han, and Wenbin Hu

This manuscript has been accepted after peer review and appears as an Accepted Article online prior to editing, proofing, and formal publication of the final Version of Record (VoR). This work is currently citable by using the Digital Object Identifier (DOI) given below. The VoR will be published online in Early View as soon as possible and may be different to this Accepted Article as a result of editing. Readers should obtain the VoR from the journal website shown below when it is published to ensure accuracy of information. The authors are responsible for the content of this Accepted Article.

To be cited as: *Chem. Asian J.* 10.1002/asia.202000504

Link to VoR: https://doi.org/10.1002/asia.202000504

A Journal of

ACES Asian Chemical Editorial Society

A sister journal of Angewandte Chemie and Chemistry – A European Journal

WILEY-VCH

10.1002/asia.202000504

WILEY-VCH

A Novel Solution-based Method for Synthesizing Pyrite-type Ferrous Metal Sulfide Microspheres with Efficient OER Activity

Wendi Xiang[a], Qianqiu Tian[a], Cheng Zhong[a,b], Yida Deng[a], Xiaopeng Han* [a,c], Wenbin Hu* [a,b]

[a] W. D. Xiang, Q. Q. Tian, C. Zhong, Y. D. Deng, X. P. Han, W. B. Hu
School of Materials Science and Engineering, Tianjin Key Laboratory of Composite and Functional Materials, Key Laboratory of Advanced Ceramics and Machining Technology (Ministry of Education)
Tianjin University
Tianjin 300072, China
E-mail: xphan@tju.edu.cn; wbhu@tju.edu.cn

[b] Joint School of National University of Singapore and Tianjin University
International Campus of Tianjin University
Binhai New City, Fuzhou 350207, China

[c] Jiangsu Key Laboratory of Electrochemical Energy-Storage Technologies, College of Materials Science and Technology, Nanjing University of Aeronautics and Astronautics, Nanjing 210016, China

Abstract: Simple and stable synthesis of transition metal sulfides and clarification of their growth mechanisms are of great importance for developing catalysts, metal-air batteries and other technologies. In this work, we develop a one-step facile hydrothermal approach to successfully synthesize NiS_2 microspheres. By changing the experimental parameters, the reason that affects the formation of nanostructured spheres is investigated and discussed in detail and the formation mechanism of microspheres is proposed innovatively. Furthermore, electrochemical testing results show that the 7h-NiS_2 catalyst exhibits remarkable oxygen evolution reaction (OER) activity with an overpotential of 311 mV at 10 mA cm^{-2} in 1.0 M KOH, superior to precious metal RuO_2. The NiS_2 catalyst also exhibits robust durability. This work will contributes to the rational design and the understanding of growth mechanism of transition metal chalcogenide electrocatalysts for diverse energy conversion technologies.

Introduction

The transition metal chalcogenides have the advantages of low cost, high abundance, good intrinsic conductivity and good structural stability [1-3]. Particularly, it has attracted extensive attentions in magnetic, optical, electrical and catalytic fields, such as catalysts, supercapacitors, lithium-ion batteries, dye-sensitized solar cells, [4, 5] etc. In recent years, some synthetic strategies, such as microwave assisted method, high temperature solid phase method and electrochemical methods, have been widely developed [6-8]. Among them, hydrothermal and solvothermal methods based synthetic strategies, under relatively low temperature and mild atmosphere, have shown unique charm in the liquid-phase synthesis of nanoparticles and the synthesis and control of low dimensional materials [9, 10]. For example, Zhang et al. synthesized a series of the Co-doped FeS_2 nanospheres, delivering discharge capacity of 0.220 Ah g^{-1} after 5000 cycles at 2 A g^{-1} with an ether-based electrolyte and in a voltage range of 0.8–2.9 V for sodium-ion batteries [11]. Moreover, a series of NiS_x (i.e., NiS, Ni_3S_2, NiS_2) nanocrystals with controllable phase and composition have been synthesized via a facile polyol solution process and the corresponding electrocatalytic properties towards oxygen evolution reaction (OER) and hydrogen evolution reaction (HER) have been systematically investigated [12]. However, up to date, most synthetic strategies mainly depend on sulfur sources with low utilization, the use of surfactant or un-environmentally friendly solvent. Moreover, to the best of our knowledge, most reports mainly focused on the electrochemical performance, while few systematic studies have been conducted on the discussion about the growth mechanism of metal sulfide materials. One of the major constraints is the reaction process cannot be directly observed in solvothermal reactions and the complexity of the multiple crystal forms of nickel sulfide systems, making it rather difficult to excavate the growth mechanism of this type of material. Therefore, it is still a challenge to synthesize phase-pure pyrite-type disulfides with a simple, universal and green method and explain its growth mechanism under mild environments.

In this work, we present a one-step facile solvothermal strategy to successfully prepare NiS_2 and CoS_2 microspheres. In contrast to the conventional approach, our approach does not require complex precursors or polluting solvent and the morphologies of the products are well controlled. Moreover, a growth mechanism of the pyrite-type disulfides microspheres has been proposed by adjusting the added ratio of sulfur to nickel in the raw materials, reaction time and solvent ratio. Electrochemical testing results indicated that the 7h-NiS_2 microspheres exhibited the best catalytic activities: overpotentials of 311 mV to achieve a current density of 10 mA cm^{-2} in 1.0 M KOH for OER. The 7h-NiS_2 microspheres also exhibited long-term catalytic durability. This work not only contributes to the controllable synthesis strategy of pyrite-type disulfides electrode materials, but also provides deeper understanding of the nucleation reaction and growth mechanism.

Results and Discussion

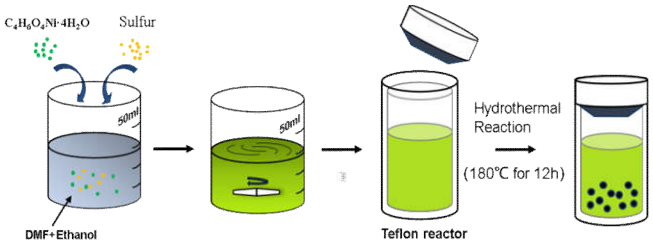

Figure 1. Schematic illustrating the preparation process of NiS_2 microsphere.

This article is protected by copyright. All rights reserved.

Accepted Manuscript

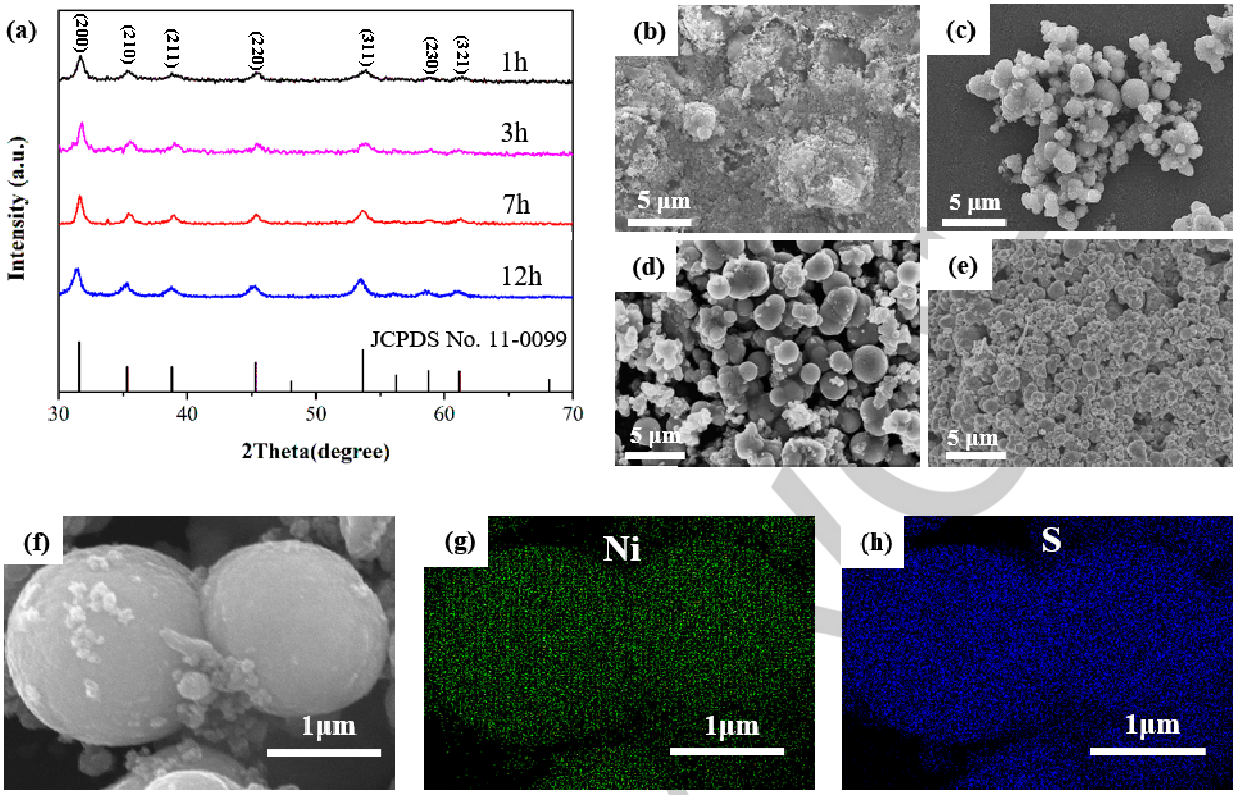

Figure 2. (a) XRD patterns of the NiS_2 with different reaction time. (b-e) SEM images of the NiS_2 with different reaction time: (b) 1h, (c) 3h, (d) 7h, and (e) 12h. (f-h) EDS mapping images of NiS_2 sample with reaction time of 7h.

A schematic illustration for the preparation process is demonstrated in Fig. 1 and the detailed programmed temperature and time are also shown (Note: room temperature was set to be 25 °C and the heating rate was constant. When they reached the set temperature, it was held for 12h). In our synthesis strategy, sulfur powder and Ni $(CH_3COO)_2{\cdot}4H_2O$ were used as the sulfur resource and the Ni resource to synthesize NiS_2. N, N-Dimethylformamide (DMF) and ethanol were selected as solvents. Most synthesis methods took complex molecular precursor [13], surfactant [14] or un-environmentally friendly solvent [11] as the raw material. Compared with them, the solvents used in our synthesis strategy have a relatively low toxicity, viscosity and cost. This also improves the security and convenience in the experimental operation process. In comparison to CS_2 [15], thiourea [16], and other sulfur sources, the use of sulfur powder can improve the utilization rate of sulfur element. In addition, the mechanism of Oswald ripening and the coordination between DMF and Ni ions are involved in the synthesis process. Because Fe^{2+}, Co^{2+} and Ni^{2+} have similar properties and can coordinate with DMF, the method and growth mechanism are expected to be suitable for synthesizing other pyrite-type disulfides.

As shown in Fig. 2, X-ray diffraction (XRD) was employed to analyze the phase and purity of the product. All diffraction peaks belong to cubic NiS_2 (JCPDS 11-0099), similar to the previous report about Ni-based system [12]. Moreover, energy dispersive spectroscopy (EDS) was performed to determine the chemical composition. The results reveal that no other element was observed except Ni and S (Fig. S1). Furthermore, the quantification of the peaks shows that the molar ratio of S and Ni is 2.02, which is quite close to the stoichiometric value of NiS_2. The scanning electron microscopy (SEM) images of the as-prepared NiS_2 for different reaction time (1, 3, 7, 12 h) were displayed in Fig. 2b–e and S2. SEM images reveal a high similarity in morphology and structure of different samples, which are composed of numerous interconnected spheres with typical average diameter of 150 nm, 600 nm, 1 μm and 1.6 μm for 1h-NiS_2, 3h-NiS_2, 7h-NiS_2 and 12h-NiS_2, respectively. The detailed morphology and structural features of NiS_2 were further demonstrated by TEM measurement (Fig. S3a and S3b). TEM results of NiS_2 showed the shape of the microspheres connected to each other and both solid spheres and a small amount of core-shell hollow spheres were observed. Moreover, HRTEM image show that observed neighbouring distances of approximately 0.326 nm correspond to the distances of the (230) planes of NiS_2; 0.143 nm and 0.151nm correspond to the distances of the (121) and (311) planes of sulfur, respectively (Fig. S3c). It can be seen some residual sulfur still existed. According to the elemental mapping of NiS_2 (Fig. 1f-h), the Ni (green) and S (blue) distribute homogeneously. In order to explain the internal structure of the microsphere, the cross section of a NiS_2 microsphere was observed. TEM images were taken on the grinded NiS_2 microsphere, showing that the inner structure of NiS_2 microspheres is composed of tiny NiS_2 nanocrystallites with an average size of 30–50 nm (Fig. S4).

X-ray photoelectron spectroscopy (XPS) was employed to characterize the chemical states and surface valence states of the prepared samples. The collected chemical compositions are consistent with the results from EDS (Fig. S5a). The Ni 2p spectra of NiS_2 are consisted of two shakeup satellites and four primary core level peaks (Fig. S5b). The peaks located at 869.2 eV and 872.85 eV are assigned to $Ni_{1/2}$ of Ni^{2+} and Ni^{3+},

This article is protected by copyright. All rights reserved.

Accepted Manuscript

respectively [8, 17]. The peaks located at 852.05 eV and 855.04 eV are assigned to the Ni $2p_{3/2}$ peaks of Ni^{2+} and Ni^{3+}. Other peaks at 859.17 and 878.22 eV are shakeup satellites, indicating the existence of the Ni^{2+} oxidation state. Fig. S5c shows the S 2p spectra. The peak appearing at binding energy of 160.04 eV is assigned to S^{2-} and the peak at 162.01 eV corresponds to S_2^{2-} of S $2p_{3/2}$. The other two fitting peaks at 160.89 and 163.05 eV are ascribed to the S $2p_{1/2}$ of S^{2-} and S_2^{2-}. The peaks at 167.2 eV and 168.3 eV are assigned to the S $2p_{3/2}$ and S $2p_{1/2}$ of S-O bond [18-21]. Accordingly, it can be concluded that the NiS_2 sample contain Ni^{2+}, Ni^{3+}, S^{2-} and S_2^{2-}, in accordance with the previous observations in the literature [22].

Optical absorption spectrum of NiS_2 was shown in Fig. S6. The spectrum was analyzed to acquire the band-gap energy (E_{bg}) of the NiS_2 by Tauc's formula. Tauc's formula shows the relationship between the absorption coefficient and the incident photon energy [23, 24], which is illustrated by $\alpha h\nu = A(h\nu - Eg)^n$, Where 'α' is the absorption coefficient, 'A' is a constant, and n = 1/2 (for a direct transition semiconductor) or n = 2 (for indirect transition semiconductors). From the chart inserted into Figure S6, the value of the E_{bg} was found to be ~ 2.74 eV, which is in good accordance with the band structure of NiS_2 [23, 24]. To investigate the porous characteristics of the NiS_2, the nitrogen adsorption and desorption isotherms was carried out at 77 K. The hysteresis loop presented in Fig. S7 can be classified as type IV and the Brunauer-Emmett-Teller (BET) surface area is determined to be about 35 $m^2 g^{-1}$, which can be possibly further enhanced by introducing nano/mesopore structures.

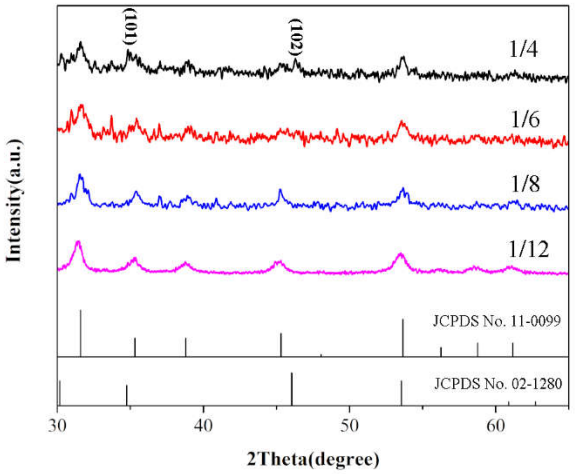

Figure 3. XRD pattern of the NiS_2 with different Ni/S molar ratios. The bottoms show the standard peaks of NiS and NiS_2.

The Ni/S molar ratio has an important effect on the morphology and phase of the product. The powder XRD patterns of the NiS_2 with different Ni/S molar ratios were shown in Fig. 3. For the samples prepared with high sulfur content (1/12, 1/8), all the diffraction peaks can be indexed to the cubic NiS_2 phase (JCPDS 11-0099). As the Ni/S molar ratio decreased to 1/6 and 1/4, the diffraction peaks are assigned to the hexagonal NiS (JCPDS no.02-1280) and the cubic NiS_2 phase (JCPDS 11-0099). Since no strong reducing agents were added in reaction, it is thought that DMF and ethanol can act as reducing agent at high temperature [25-28]. Therefore, sulfur can be reduced to S^{2-} in solvents and then form S_2^{2-} with the surplus of sulfur and finally react with Ni^{2+} to form NiS_2. As the Ni/S molar ratio increased, a part of S^{2-} cannot be reduced to S_2^{2-}. Instead, NiS was generated via combining S^{2-} with Ni^{2+}. Therefore, diffraction peaks of NiS ((101), (102)) were observed in sample 1/4 and 1/6.

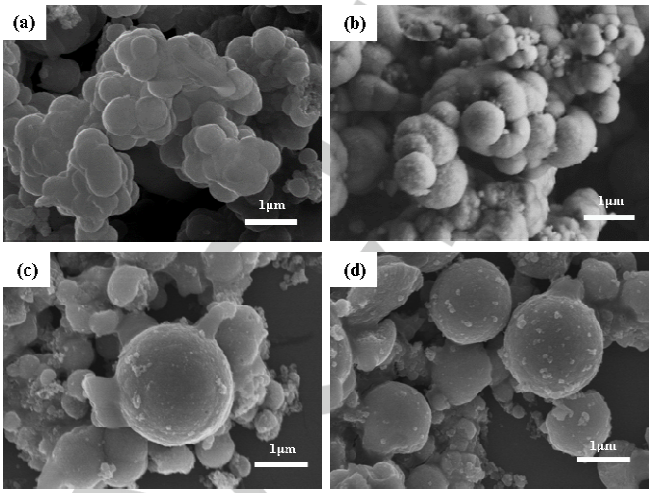

Figure 4. SEM images of NiS_2 with different Ni/S ratios: (a) 1/4, (b) 1/6, (c) 1/8, (d) 1/12.

As shown in Fig. 4 and S8, large quantities of spheres with diameters of approximately 500 nm–1.7 μm were observed. The smaller nanospheres coalesced and stacked together irregularly to form bulky nanostructures with 1/4 Ni/S molar ratio. With Ni/S molar ratio decreased, the bonding between the spheres is closer and tends to reunite into larger spheres (Fig. 4b). Thus, the decreased Ni/S molar ratio leads to the increased diameter of the final microspheres until to the maximal size, which is determined by the aggregation barrier of the system (Fig. 4c and d) [29]. It can be clearly seen that as the sulfur content increases, small spheres gradually integrated into large spheres. On the basis of the above analysis, it is believed that Ostwald ripening play an important role in NiS_2 growth process [30, 31]. In this process, small-sized NiS_2 microspheres gradually disappeared and accompanied by the growth of large-sized microspheres. Moreover, sulfur is liquid at 180 °C with fluidity and viscosity and it tends to form a spherical surface to reduce the surface energy of the system. Therefore, with the sulfur content increases, the aggregation of sulfur droplets becomes more intense, resulting in the generation of larger NiS_2 microspheres.

In this binary solution system, the phase and the morphology of the products are strongly influenced by used solvents of DMF or ethanol. The XRD patterns of prepared samples in a mixed solvent of DMF and ethanol (volume ratio is 1:1, Fig. 2a) indicate that the product is pure NiS_2 while other impurities will form when only use the DMF or ethanol as the solvent (Fig. 5a). The morphologies of the surfaces were characterized using scanning electron microscopy (Fig. 5b, c and Fig. S9). The DMF-only sample is composed of the accumulated microspheres but the ethanol-only sample contains a huge number of chunks and irregular particles. Moreover, DMF and ethanol act as reducing agents to provide S^{2-} for the nucleation reaction. At the same time, sulfur atoms can replace oxygen atoms in DMF to form N, N-dimethylthioamide at high temperature [32]. When using only DMF, a large amount of sulfur is consumed via the above reaction, so that S^{2-} can't be converted into S_2^{2-} completely. Therefore, the phase of NiS appeared in XRD pattern of DMF-only samples. In addition to being used as a reducing agent and

This article is protected by copyright. All rights reserved.

Accepted Manuscript

a reaction raw mate-rial, DMF is also used as a ligand for Ni^{2+}. It has been reported that DMF is O-bonded to nickel as coordination via nitrogen and it is believed that DMF plays an important role in controlling precipitation processes [33]. The sample without DMF presents irregular bulk aggregations, which may be attributed to the fast reaction between Ni^{2+} and S_2^{2-}. Herein, another function of DMF is to form a complex with Ni^{2+} ions through a coordination interaction that controls the release rate of Ni^{2+} from the complex, thus reducing the precipitation rate of NiS_2 and enhancing the product regularity [34, 35]. As shown in Figure S10, DMF shows characteristic absorption bands at 1660 and 655 cm^{-1} [36]. When DMF binds to Ni^{2+}, the band at 1660 cm^{-1} shifts to 1659.16 cm^{-1} due to the weakening of the double-bond nature of the carbonyl bond. Meanwhile, the peak at 655.8 cm^{-1} shifts to 658.28 cm^{-1}, possibly due to the increase in the order of the amide C-N bond [37, 38]. It should be noted that a new peak appear at 410.47 cm^{-1}, which can be attributed to Ni-O bond formation [39].

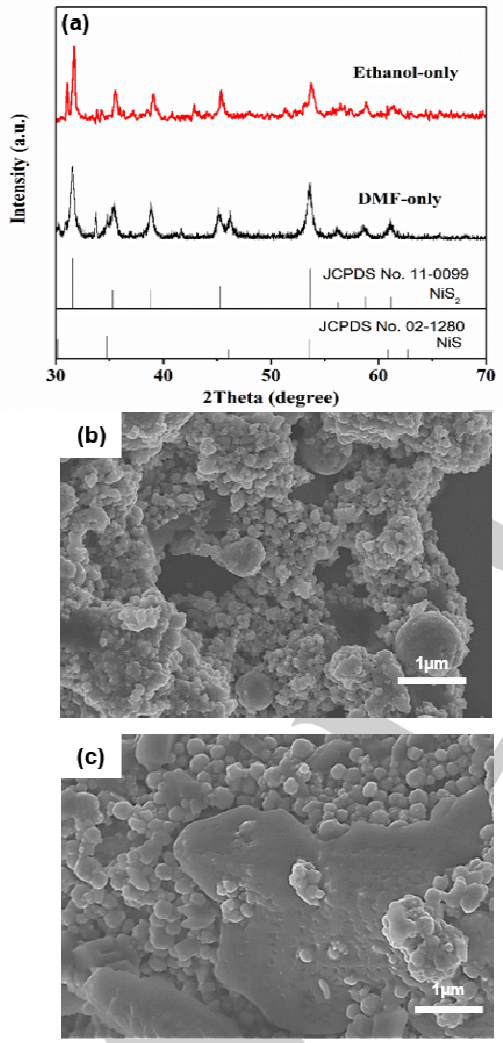

Figure 5. XRD pattern (a) and SEM images of prepared samples with solvent of (b) DMF-only, (c) ethanol-only.

Thermogravimetric analysis (TGA) was performed to characterize the thermal stability. The TGA curve in Fig. 6 reveals a 53 % weight loss of the NiS_2 sample in total, which is composed of 10 % weight loss of residual H_2O and DMF between 70 °C and 110 °C at first and then a 21.53 % weight loss of sulfur between 220 °C and 340 °C later on [40]. A final 20.72 % weight loss between 380 °C to 550 °C is observed and the phase of the residues collected after calcination at 380 °C for 2 h has also been examined. The XRD patterns in Figure S11 indicated that the product collected after 380 °C treatment was a mixture of $Ni_{0.96}S$ and NiS_2 phases. In the differential scanning calorimetry (DSC) curve, the endothermic peaks around 90 °C and 120 °C are attributed to the residual H_2O and DMF. The peaks between 260 °C and 300 °C present the violent volatilization of sulfur and the peak between 350 °C to 550 °C is endothermic caused by the decomposition of NiS_2. The above analysis indicates that the prepared NiS_2 sample contains a certain amount of sulfur. This is ascribed to the use of excess sulfur powder during the solvothermal reaction, which will be further optimized in the next research stage.

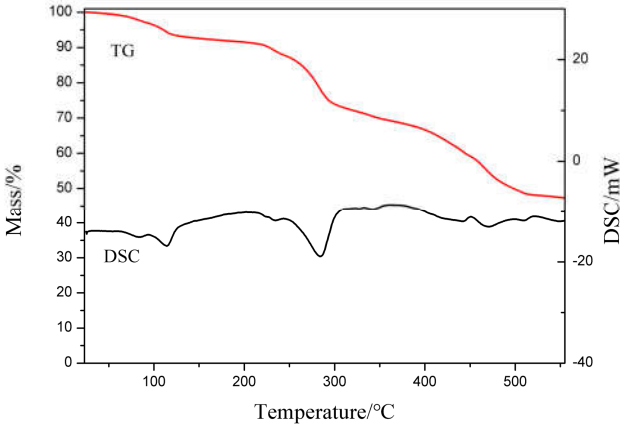

Figure 6. TG and DSC curves of the 12h-NiS_2 under N_2 flow with a heating rate of 10 °C min^{-1}.

During the synthesis, the NiS_2 nanospheres constructed by nanocrystalline grains can be obtained through a hydrothermal process. In the reaction, the Ni^{2+}, DMF, ethanol and sulfur can form a similar oil/water system. DMF and ethanol react with sulfur to release S^{2-} at the DMF/sulfur interface and S^{2-} react with sulfur to generate S_2^{2-} to provide sulfur source for the formation of NiS_2. The whole reaction can be simplified as the following :

$$S\ (DMF, ethanol) \rightarrow S^{2-} \quad (1)$$

$$S^{2-} + S \rightarrow S_2^{2-} \quad (2)$$

$$Ni^{2+} + S_2^{2-} \rightarrow NiS_2 \quad (3)$$

Based on the above experimental observations, a plausible formation mechanism of the pyrite-type disulfides microspheres is proposed and illustrated in Fig. 7. The formation process mainly can be divided into three stages, including the formation of DMF-Sulfur system, crystallization processes and growing processes. Firstly, DMF is a strong Lewis base known to form bond with metallic cation via its oxygen atom and it coordinate with Ni^{2+} to form a stable $[Ni(dmf)_6]^{2+}$ complex [41-43]. After the temperature rises to 180 °C, the sulfur is converted into a liquid state and forms a liquid-liquid heterogeneous solution with DMF. During the middle stage of the hydrothermal process, the DMF can carry Ni^{2+} from the solvent phase to the Liquid-liquid interface. The DMF reacts with sulfur to release S_2^{2-}, and then reacts with Ni^{2+} to form NiS_2 nuclei. Afterwards, NiS_2 nanocrystalline is aggregated or coalesced to assemble the NiS_2 microspheres due to van der Waals force (intermolecular force) and violent collisions caused by Brownian motion [44, 45]. Lastly, Ostwald ripening process proceeded, eliminating crystallites of

This article is protected by copyright. All rights reserved.

Accepted Manuscript

smaller sizes. Whilst the growth of the larger ones moves along, the morphology of interconnected microspheres is finally formed.

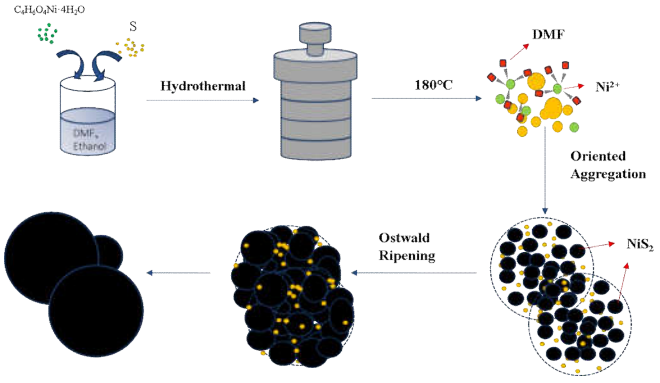

Figure 7. Schematic illustration of formation mechanism of NiS_2 microspheres.

To further demonstrate the versatility of this method, we extended the synthesis to preparation of other ferrous metal sulfide materials. The example of CoS_2 microspheres shown in Fig. S12 and S13 is a testament to the feasibility and generality of this approach in controlling the morphology of pyrite-type disulfides. XRD was used to analyze the phase and purity of the product. All diffraction peaks of the samples are assigned to cubic CoS_2 (JCPDS 41-1471). EDS was performed to determine the chemical composition. The results reveal that no other element was observed except Co and S (Fig. S12). Furthermore, the quantification of the peaks shows that the molar ratio of S to Co is 1.9, agreeing with the standard value of CoS_2. SEM images indicate the microsphere structure morphology of prepared CoS_2 that is very similar to that of NiS_2 (Fig. S13).

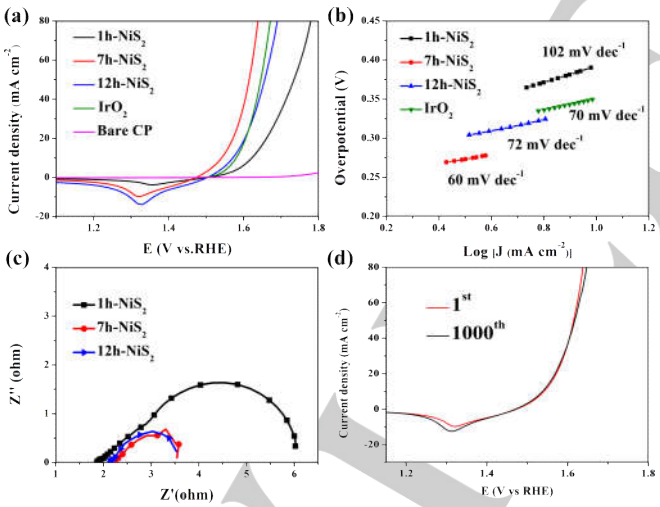

Figure 8. (a) OER polarization curves of Bare CP, 12h-NiS_2, 7h-NiS_2, 1h-NiS_2, and IrO_2 in 1.0 M KOH at a scanning rate of 5mV s^{-1}. (b) Tafel plots of 12h-NiS_2, 7h-NiS_2, 1h-NiS_2, and IrO_2. (c) EIS spectra of 12h-NiS_2, 7h-NiS_2 and 1h-NiS_2. (d) Catalytic durability of 7h-NiS_2.

The electrochemical properties of the NiS_2 sample were further evaluated. The NiS_2 synthesized at three different reaction times were evenly spread onto 1 × 1 cm carbon paper (CP), and then the catalyst-modified CP was used as the working electrode. The performance of the bare CP and IrO_2 was also tested for comparison. Fig. 8a displays the OER polarization curves in 1.0 M KOH at 5 mV s^{-1}. Specifically, to reach an anodic current density of 10 mA cm^{-2}, the 7h-NiS_2 catalyst exhibits a considerable overpotential of 311 mV (Table 1), which is lower than those of 12h-NiS_2 (341 mV) and 1h-NiS_2 (390 mV) and the precious metal IrO_2 catalyst (350 mV). Moreover, the Tafel slope of the 7h-NiS_2 electrode is fitted to be 60 mV dec^{-1} (Fig. 8b), which is smaller than those of 12h-NiS_2 (72 mV dec^{-1}), 1h-NiS_2 (102 mV dec^{-1}) and IrO_2 (70 mV dec^{-1}). It has been widely accepted that, the elementary reaction steps of the complete OER mechanism in alkaline solution are as follows [46]: (1) $M + OH^- \rightarrow MOH + e^-$, (2) $OH^- + MOH \rightarrow MO + H_2O + e^-$, (3) $MO + OH^- \rightarrow MOOH + e^-$, (4) $MOOH + OH^- \rightarrow O_2 + H_2O + e^-$, where M is the active site on the surface. Generally, the smaller Tafel slope indicates faster kinetics for OER catalysis and more rapid increase in the rate of O_2 generation with the applied overpotential [47, 48]. Electrochemical impedance spectroscopy (EIS) reveals that the charge-transfer resistance (R_{ct}) values are around 4.13, 1.35 and 1.4 Ω for 1h-NiS_2, 7h-NiS_2 and 12h-NiS_2, respectively (Fig. 8c), suggesting that 7h-NiS_2 has the fastest charge transfer ability. This trend is in accordance with the polarization results and Tafel slopes. Apart from the high activity, the 7h-NiS_2 catalyst also exhibits catalytic durability which is further corroborated by the overlaid OER curves after the 1st and 1000th cyclic voltammetry (CV) cycles. XPS and HRTEM reveal that an amorphous oxide layer appears after 1000 OER cycles (Fig. S14 and S15), consistent with previous literatures [49-52]. Among different samples, 7h-NiS_2 shows the best performance for OER in alkaline media and is comparable to many previously reported Ni sulfides (Table 2). The poor activity of 1h-NiS_2 should be due to that NiS_2 crystallized incompletely and the unreacted sulfur powder covered the OER active site after one-hour synthesis procedure. With longer reaction time, the NiS_2 microspheres gradually grew larger with the increased crystallinity and decreased content of sulfur powder. Therefore, 7h-NiS_2 shows the best performance. As the reaction continued, the specific surface area of the microspheres decreased due to the Oswald process, presenting inferior catalytic activity.

Table 1. Comparison of performance parameters of 1h-NiS_2, 7h-NiS_2 and 12h-NiS_2 in this work.

Catalysts	Reaction	Overpotential @10mA cm^{-2} (mV)	Tafel slope (mV dec^{-1})	R_{ct} (Ω)
1h-NiS_2	OER	390	101	4.13
7h-NiS_2	OER	311	60	1.35
12h-NiS_2	OER	341	72	1.41
IrO_2	OER	350	70	

Table 2. Comparison of OER performance parameters in this work with the results in references.

Catalysts	Support	Electrolyte	Current density (mA cm^{-2})	Overpotential (mV)	Refs
NiS_2 microsphere	Carbon paper	1.0M KOH	10	314	This work
Nanocrystalline NiS particles	Carbon paper	1.0M KOH	10	345	53
NiS_2 hollow microspheres	Carbon paper	1.0 M KOH	10	320	54

This article is protected by copyright. All rights reserved.

Accepted Manuscript

Ni@NiO@C	Copper foil	1.0 M KOH	10	380	55
N-doped Ni_3S_2	Nickel foam	1.0 M KOH	100	330	56
NiS_2 nanocatalysts	Carbon paper	1.0 M KOH	10	375	12
$Ni_{0.85}Se$ films	Glassy carbon	1.0 M NaOH	10	320	57
NiS spheres	Nickel foam	1.0M KOH	50	335	58

Conclusion

In conclusion, we have successfully synthesized NiS_2 microspheres using a new one-step facile solution-based strategy. This method is simple, cheap, green, non-toxic and easy to operate due to the low viscosity of the solution. In addition, the route for the synthesis of NiS_2 microstructures will be a promising way in the industrial application of pyrite-type disulfides. Among prepared products, the 7h-NiS_2 exhibits the best catalytic activity with low overpotential of 311 mV to achieve a current density of 10 mA cm^{-2} for OER and remarkable long-term catalytic durability. Besides, it was found that the formation of NiS_2 microspheres was attributed to the oriented aggregations and the Ostwald ripening. The work provides insight into the controlled synthetic mechanism of earth-abundant transition metal sulfide based compounds.

Experimental Section

Materials synthesis

In this work, NiS_2 microspheres are synthesized by a solvothermal method. The specific steps are as follows: 0.246 g $Ni(CH_3COO)_2{\cdot}4H_2O$ is weighed and dissolved in the mixed solution of 15 ml ethanol and 15 ml DMF, followed by magnetic stirring for 30 minutes. Then, 0.39 g sulfur powder is added into the solution and stirred for 30 minutes to form a uniform mixture. The autoclave is placed in a furnace and then the temperature is evaluated to 180 °C at a rate of 10 °C/min and maintained for 12 h. After naturally cooling to room temperature, the samples are separated by centrifugation, washed using deionized water and ethanol for three times. Finally, the NiS_2 product is collected after lyophilizing. The synthetic procedure for CoS_2 is similar to that of NiS_2 except replacing the Ni $(CH_3COO)_2{\cdot}4H_2O$ by the same molar amount of $Co(CH_3COO)_2{\cdot}4H_2O$.

Materials Characterization

The synthesized compounds are characterized by X-ray diffraction (XRD) which are produced by Bruker/D8 Advanced with Cu Kα radiation source (λ=0.15418 nm) and X-ray photoelectron spectroscope (XPS) which are collected by an Escalab 250Xi. The morphologies and elemental analysis of samples are studied by scanning electron microscopy (SEM, Hitachi s4800, 30KV) and transmission electron microscopy (TEM, JEOL JEM-2100F, 200KV). Brunauer Emmett Teller (BET) is measured by an AutosorbiQ instrument (Quantachrome U.S.). The absorption spectra of the NiS_2 microspheres were measured using a UV-Vis spectrometer (Hitachi U-3300) with an integrated sphere. TG and DSC curves were obtained by using a TG-DSC 6300 Mettler Toledo. The purge gas was nitrogen with a flow rate of 100 mL min^{-1} and a heating rate of 10 °C min^{-1} was adopted.

Electrocatalytic Measurements

The electrochemical measurement is tested using the Iviumstat electrochemical workstation. The OER performances are measured in a three electrodes system in a 1.0 M KOH electrolyte, platinum electrode and saturated calomel electrode (SCE) are used as counter electrode and reference electrode, respectively and prepared samples are designed as working electrode. For making the working electrode for OER, first to dispose the CP and mix 10 mg NiS_2 samples into 960μl isopropanol, then add 35 μl Nafion to form a homogeneous solution. The working electrode is a CP (1 cm*1 cm) covered with 150 μl prepared solution. Cyclic voltammograms (CV) are conducted firstly to reach a steady state. The linear sweep voltammetry (LSV) curves of OER LSV curves are at 0.9 V ~ 0 V and the scanning speed is 5 mV s^{-1}. The collected data is calculated according to the iR-compensation, the equation is $E_{corr} = E_{mea} - iR_s$. And all data is transformed to reversible hydrogen electrode (RHE) following the equation $E_{vs.\ RHE} = E_{vs.\ SCE} + 0.059 * pH + 0.241$.[59-61] Electrochemical impedance spectroscopy (EIS) is measured with the frequencies from 10 kHz to 0.01 Hz. To testify the stability of samples, ChronoPotentiometry data at 10 mA cm^{-2} current density is collected.

Acknowledgements

This work was supported by the Young Elite Scientists Sponsorship Program by CAST (2018QNRC001), the National Natural Science Foundation of China (51972224, U1601216), and the Tianjin Natural Science Foundation (17JCQNJC02100).

Keywords: SOLVOTHERMAL SYNTHESIS•GROWTH MECHANISM•OXYGEN EVOLUTION•METAL SULFIDE•MICROSPHERES

[1] X. Wu, X. Han, X. Ma, W. Zhang, Y. Deng, C. Zhong, *ACS Appl. Mater. Interfaces* **2017**, *9*, 12574-12583.
[2] S. Hong, D. Fu, J. Hou, D. Zhou, B. Wang, Y. Sun, P. Liu, *Sci. China Mater.* **2018**, *54*,169-173.
[3] D. Liu, Y. Tong, X. Yan, J. Liang, S. X. Dou, *Batteries&Supercaps* **2019**, *2*, 743.
[4] H. Wang, Y. Liang, Y. Li, H. Dai, *Angew. Chem. Int. Ed.* **2011**, *123*, 11161-11164.
[5] J. Y. Hwang, S. Myung, Y. K. Sun, *Chem. Soc. Rev.* **2017**, *10*.1039.
[6] Z. W. Seh, J. Yu, W. Li, H. Wang, Y. Sun, H. Yao, Y. Cui, *Nat. Commun.* **2014**, *5*, 5017.
[7] Q. Lu, Y. Yu, Q. Ma, B. Chen, H. Zhang, *Adv. Mater.* **2016**, *28*, 1917-1933.
[8] X. Ma, W. Zhang, Y. Deng, C. Zhong, W. Hu, X. Han, *Nanoscale* **2018**, *10*, 1039.
[9] V. Valtchev, L. Tosheva, *Chem. Rev*. **2013**. *113*, 6734-6760.
[10] D. Liang, Z. Lu, H. Yang, J. Gao, R. Chen, *ACS Appl. Mater. Interfaces* **2016**. *8*, 10099.
[11] K. Zhang, M. Park, L. Zhou, G. Lee, Z. Hu, J. Chen, *Angew. Chem. Int. Ed*. **2016**, *55*, 12822-12826.

This article is protected by copyright. All rights reserved.

Accepted Manuscript

[12] X. Zheng, X. Han, Y. Zhang, J. Wang, C. Zhong, Y. Deng, W. Hu, *Nanoscale* **2019,** *11*, 5646-5654.
[13] X. Song, W. Shen, Z. Sun, C. Yang, P. Zhang, L. Gao, *Chem. Eng. J.* **2016**, *290*, 74-81.
[14] J. Polonský, I. M. Petrushina, E. Christensen, K. Bouzek, C. B. Prag, J. E. T. Andersen, N. J. Bjerrum, *Int. J. Hydrogen. Energy* **2012**, *37*, 2173-2181.
[15] S. Peng, L. Lin, H. Tan, C. Ren, W. Shi, C. Li, G. M. Subodh, R. Seeram, Q. Yan, *Adv. Funct. Mater.* **2014**, *24*, 2155-2162.
[16] C. D. Giovanni, A. Reyes-Carrnona, A. Coursier, S. Nowak, J. M. Greneche, H. Lecoq, L. Mouton, J. Roziere, D. Jones, J. Peron, *ACS Catal.* **2016**, 2626-2631.
[17] X. Rui, H. Tan, Q. Yan, *Nanoscale* **2014**, *6*, 9889-924.
[18] VI. Nefedov. *J. Electron. Spectrosc.* **1999**, *100*,1-15.
[19] I. K. Tamás, M. István, P. Zoltán, *J. Catal.* **1989**, *116*, 422-439.
[20] X. Wang, Q. Xiang, B. Liu, L. Wang, T. Luo, D. Chen, G. Shen, *Sci. Rep.* **2013**, *3*, 2007.
[21] Q. Liu, J. Jin, J. Zhang, *ACS Appl. Mater. Interfaces* **2013**, *5*, 5002–5008.
[22] X. Zheng, Y. Zhang, H. Liu, D. Fu, J. Chen, J. Wang, C. Zhong, Y. Deng, X. Han, W. Hu, *Small* **2018**, *14*, 1803666.
[23] M. R. Mohammed, A. Jamal, S. B. Khan, M. Faisal, *Biosens. Bioelectron.* **2011**, *28*, 127.
[24] Y. Bai, M. Yang, S. H. Cha, K. Sun, N. A. Kotov, *J. Phys. Chem. C* **2013**, *117*, 2567.
[25] M. K. Carpenter, T. E. Moylan, R. S. Kukreja, M. H. Atwan, J. *Am. Chem. Soc.* **2012**, *134*, 8535-8542.
[26] X. Tang, L. Ren, L. Sun, W. Tian, M. Cao, C. Hu, *Chem. Res. Chinese Univ.* **2006**, *22*, 547-551.
[27] S. Li, H. Zhang, Y. Ji, D. Yang, *Nanotechnology* **2004**, *15*, 1428-1432.
[28] Y. Chang, J. J. Teo, H. Zeng, *Langmuir* **2005**, *21*, 1074-1079.
[29] J. Polte, *CrystEngComm.* **2015**, *17*, 6809-6830.
[30] H. Zeng, *J. Mater Chem.* **2006**, *16*, 649-662
[31] J. Liu, D. Xue, *J. Cryst. Growth.* **2009**, *311*, 500-503.
[32] Y. Qu, Z. Li, H. Xiang, X. Zhou, *Adv. Synth. Catal.* **2013**, *16*, 3141‑3146.
[33] U. Yasuhiro, M. Kai, M. Watanabe, K. Katoh, *Anal. Sci.* **2001**, *2*, 323-326.
[34] H. Zhang, W. Li, M. Jin, J. Zeng, T. Yu, D. Yang, Y. Xia, *Nano Lett.* **2011**, *11*, 898–903.
[35] Y. Xiong, H. Cai, B. Wiley, J. Wang, M. J. Kim, Y, Xia, *J. Am. Chem. Soc.* **2007**, *12*, 3665-3675.
[36] Y. J. Kim, C. R. Park, *Inorg. Chem.* **2002**, *41*, 6211-6216.
[37] Y. T. Yilmaz, Y. Topcu, *Thermochim. Acta.* **1997**, *307*, 143-147.
[38] E. W. Randall, C. M. S Yoder, J. J Zuckerman, *Inorg. Chem.* **1966**, *5*, 2240-2242.
[39] J. Li, H. J. Zhang, J. Chang, *Crystals* **2018**, *8*, 176.
[40] M. Zhang, W. Zhu, S. Xun, Q. Wang, *Chem. Eng. J.* **2013**, *6*, 328–336.
[41] M. C. Das, H. Xu, Z. Wang, W. Zhou, Y. Yue, G. Qian, B. Chen, *Chem Commun.* **2011**, *47*, 11715-7.
[42] R. álvarez, M. PeRez, O. N. Faza, D. Lera, *Organometallics.* **2008**, *27*, 3378-3389.
[43] R. W. Hay, S. Albedyhl, P. Lightfoot, *Transit. Metal. Chem.* **1998**, *23*, 257-260.
[44] J. Polte, R. Erler, A. F. Thünemann, F. Emmerling, R. Kraehnert, *Chem. Commun.* **2010**, *46*, 9209.
[45] J. F. Kettemann, M. Wuithschick, G. Caputo, R. Kraehnert, N. Pinna, K. Rademann, *Crystengcomm* **2015**, *8*, 238-243.
[46] T. Shinagawa, A. T. Garcia-Esparza, K. Takanabe, *Sci. Rep.* **2015**, *5*, 13801.
[47] J. Hu, J. Zhang, C. Cao, *Int. J. Hydrogen. Energy* **2004**, *8*, 791-797.
[48] J. Polonský, I. M. Petrushina, E. Christensen, K. Bouzek, C. B. Prag, J. E. T. Andersen, N. J. Bjerrum, *Int. J. Hydrogen. Energy* **2012**, *37*, 2173-2181.
[49] H. Sun, X. Xu, Z. Yan, X. Chen, F. Cheng, P. S. Weiss, J. *Chen, Chem. Mater.* **2017**, *29*, 8539–8547.
[50] S. Jin, *ACS Energy Lett.* **2017**, *2*, 1937–1938.
[51] X. Han, X. Wu, Y. Deng, J. Liu, J. Lu, C. Zhong, W. Hu, *Adv. Energy Mater.* **2018**, *8*, 1800935.
[52] W. Zhao, X. Mu, P. He, H. Zhou, *Batteries&Supercaps* **2019**, *2*, 803.
[53] W. Dai, Y. Pan, N. Wang, S. Wu, X. Li, Y. Zhu, *Mater. Lett.* **2018**, *218*, 115-118.
[54] P. Luo, H. Zhang, L. Liu, Y. Zhang, J. Deng, C. Xu, N. Hu, Y. Wang, *ACS Appl. Mater. Interfaces* **2017**, *9*, 2500.
[55] D. Xu, C. Mu, B. Wang, J. Xiang, W. Ruan, F. Wen, X. Du, Z. Liu, Y. Tian, *Sci. China Mater.* **2017**, *60*, 947-954.
[56] P. Chen, T. Zhou, M. Zhang, Y. Tong, C. Zhong, N. Zhang, *Adv. Mater.* **2017**, *29*, 1701584.
[57] X. Wu, D. He, H. Zhang, H. Li, Z. Li, B. Yang, *Int. J. Hydrogen. Energy* **2016**, *41*, 10688-10694.
[58] W. Zhu, X. Yue, W. Zhang, S. Yu, J. Wang, *Chem. Commun.* **2015**, *52*, 1486.
[59] X. Han, X. Ling, D. Yu, D. Xie, L. Li, S. Peng, C. Zhong, N. Zhao, Y. Deng, W. Hu, *Adv. Mater.* **2019**, *31*, 1905622.
[60] S. Zhao, B. Qin, K.-Y. Chan, C.-Y. V. Li, F. Li, *Batteries & Supercaps* **2019**, *2*, 725.
[61] Z. Zhang, X. Li, C. Zhong, N. Zhao, Y. Deng, X. Han, W. Hu, *Angew. Chem. Int. Ed.* **2020**, *59*, 7245.

This article is protected by copyright. All rights reserved.

Accepted Manuscript

10.1002/asia.202000504

Entry for the Table of Contents

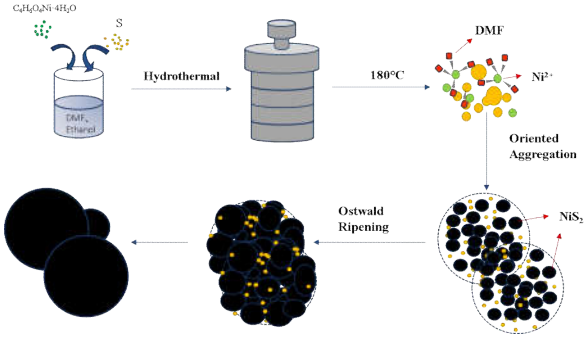

NiS_2 and CoS_2 microspheres were prepared by a one-step facile solvothermal strategy. In contrast to the conventional approach, this method does not require complex precursors or polluting solvent and the morphologies of the products are well controlled. Moreover, a growth mechanism of the pyrite-type disulfides microspheres has been proposed. Electrochemical testing results indicated that the 7h-NiS_2 microspheres exhibited the best OER catalytic activities with overpotential of 311 mV to achieve a current density of 10 mA cm^{-2} in 1.0 M KOH as well as robust long-term durability.

WILEY-VCH

Accepted Manuscript

This article is protected by copyright. All rights reserved.